ACS OMEGA

http://pubs.acs.org/journal/acsodf

Article

Optimizing TiO_2 through Water-Soluble Ti Complexes as Raw Material for Controlling Particle Size and Distribution of Synthesized $BaTiO_3$ Nanocubes

Kouichi Nakashima,* Kouta Hironaka, Kazuma Oouchi, Mao Ajioka, Yoshio Kobayashi, Yasuhiro Yoneda, Shu Yin, Masato Kakihana, and Tohru Sekino

Cite This: *ACS Omega* 2021, 6, 32517−32527

Read Online

ACCESS | Metrics & More | Article Recommendations | Supporting Information

ABSTRACT: Barium titanate ($BaTiO_3$) nanocubes with a narrow particle size distribution were synthesized using a three-step approach. First, a water-soluble Ti complex was synthesized using a hydrolysis method. Next, the titanium dioxide (TiO_2) raw material was synthesized via a hydrothermal method using various water-soluble titanium (Ti) complexes. The TiO_2 exhibited various particle sizes and crystal structures (anatase, rutile, or brookite) depending on the water-soluble Ti complex and the hydrothermal conditions used in its synthesis. Finally, $BaTiO_3$ nanocubes were subsequently created through a hydrothermal method using the synthesized TiO_2 particles and barium hydroxide octahydrate [$Ba(OH)_2{\cdot}8H_2O$] as raw materials. The present study clarifies that the particle size of the $BaTiO_3$ nanocubes depends on the particle size of the TiO_2 raw material. $BaTiO_3$ particles with a narrow size distribution were obtained when the TiO_2 particles exhibited a narrow size distribution. We found that the best conditions for the creation of $BaTiO_3$ nanocubes using TiO_2 involved using lactic acid as a complexing agent, which resulted in a particle size of 166 nm on average. This particle size is consistent with an average of the width of the cubes measured from corner to corner diagonally, which corresponds to a side length of 117 nm. In addition, surface reconstruction of the $BaTiO_3$ was clarified via electron microscopy observations, identifying the outermost surface as a Ti layer. Electron tomography using high-angle annular dark-field (HAADF)-scanning transmission electron microscopy (STEM) confirmed the three-dimensional (3D) structure of the obtained $BaTiO_3$ nanocubes.

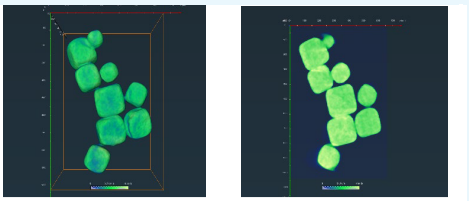

Electron tomography observations of $BaTiO_3$ nanocubes.

INTRODUCTION

Enhanced materials require a specific morphology design of their particles. The objective of the present study was the synthesis of highly dispersed barium titanate ($BaTiO_3$) nanocubes with a narrow particle size distribution[1] leading to enhanced dielectric properties.[2−4] We therefore developed a method to synthesize $BaTiO_3$ nanocubes with the aforementioned properties.

Enhanced dielectric materials require a high relative dielectric constant. To improve the relative dielectric constant, the development of a dense ceramic is necessary. High-density ceramics facilitate greater electric conductivity than low-density ceramics. $BaTiO_3$ nanocubes play an important role in dense ceramics. When the $BaTiO_3$ nanocubes with a narrow particle size distribution are accumulated, the resulting ceramic is formed with a high density. In addition, the relative dielectric constant would increase if the interface of the $BaTiO_3$ nanocube that had a wide surface area was distorted and had polarization. Therefore, the $BaTiO_3$ nanocube has a potential to lead into an enhanced dielectric material.

Titanium dioxide (TiO_2) is a famous substance for a photocatalyst. Recently, papers concerning a TiO_2-based photocatalyst were published in 2019−2021.[5−10] One of the research of the papers described highly efficient photocatalytic overall water splitting. Hydrogen and oxygen evolution with overall water splitting is the most important research in environment-harmonized materials and the clean energy demand. In this study, TiO_2 was synthesized using a hydrothermal method, and the obtained TiO_2 was used for a raw material to synthesize $BaTiO_3$ nanocubes.

Our synthesis of $BaTiO_3$ nanocubes is based on a hydrothermal method that enables control of the particle morphology. In addition, we developed a comprehensive scheme for the synthesis of $BaTiO_3$ nanocubes using TiO_2 synthesized in situ as a raw material. We speculated that highly dispersed $BaTiO_3$ nanocubes with a narrow size distribution would be obtained if TiO_2 that is also highly dispersed and exhibits a narrow size distribution was used as a raw material. The key to our approach is the use of a water-soluble titanium (Ti) complex for the synthesis of TiO_2,[11−21] which leads to the

Received: July 27, 2021
Accepted: November 2, 2021
Published: November 24, 2021

https://doi.org/10.1021/acsomega.1c04013
ACS Omega 2021, 6, 32517−32527

synthesis of TiO_2 particles with various sizes and structures. Previous papers reported the synthesis method of water-soluble Ti complexes using various ligands such as glycolic acid, lactic acid, and citric acid. Crystal structures of $(NH_4)_6[Ti_4(C_2H_2O_3)_4(C_2H_3O_3)_2(O_2)_4O_2]$, $(NH_4)_2[Ti(C_3H_4O_3)_3]$, and $(NH_4)_8[Ti_4(C_6H_4O_7)_4(O_2)_4(O_2)_4]\cdot 8H_2O$ were described in detail. Moreover, TiO_2 with various crystal structures such as anatase-type, rutile-type, and brookite-type was obtained using a solvothermal method. The required properties of the TiO_2 nanocrystals in this study are summarized as follows:

1. Highly dispersed particles less than 25 nm in size
   Reason 1: Anatase-type TiO_2 with highly dispersed particles smaller than 25 nm is difficult to source commercially because the nanoparticles tend to aggregate.
   Reason 2: $BaTiO_3$ nanocubes with a narrow particle size distribution would be obtained if highly dispersed anatase-type TiO_2 particles smaller than 25 nm were used as a raw material.
2. Crystal structure: anatase-type, rutile-type, and brookite-type
   Reason: The effect of the structure of TiO_2 as a raw material on the morphology of $BaTiO_3$ is unknown.

We can obtain anatase-type TiO_2 below 25 nm from pharmaceutical companies. However, it is difficult to purchase finer particles with dispersion. In addition, the effect of the structure of TiO_2 as a raw material on the morphology of $BaTiO_3$ is unknown. We theorized that the intermediate complex and the dissolving speed were different when anatase-type, rutile-type, and brookite-type TiO_2 particles were dissolved in reaction media. Accordingly, $BaTiO_3$ nanocubes with a narrow particle size distribution would be obtained if highly dispersed anatase-type, rutile-type, or brookite-type TiO_2 particles smaller than 25 nm were used as the raw material.

$BaTiO_3$ nanocubes were hydrothermally synthesized using TiO_2 nanoparticles made in situ. Controlling nucleation and crystal growth of $BaTiO_3$ nanocubes was recently published for the solvothermal synthesis of $BaTiO_3$ nanocubes.[1] This paper described varying the ratio of titanium tetraisopropoxide $\{[(CH_3)_2CHO]_4Ti\}$ and TiO_2 as raw materials, where the $[(CH_3)_2CHO]_4Ti$ encouraged nucleation and the fine TiO_2 nanoparticles boosted crystal growth. In this previous paper, commercial TiO_2 nanoparticles were used for the synthesis of $BaTiO_3$ nanocubes. Therefore, the present study primarily focused on the raw materials used to synthesize the TiO_2 to improve the size distribution and dispersion of the $BaTiO_3$ nanocubes. In addition, detailed observations of the surface of the $BaTiO_3$ nanocubes were done by electron microscopy because the surface structure gave us useful information about the improved properties of the material. Our objective was to synthesize highly dispersed $BaTiO_3$ nanocubes with a narrow particle size distribution.

RESULTS AND DISCUSSION

$BaTiO_3$ was synthesized in three steps. The first step was the synthesis of a water-soluble Ti complex. The second step was hydrothermal reaction of TiO_2 using the water-soluble Ti complex. The third step was the hydrothermal synthesis of $BaTiO_3$ using the synthesized TiO_2.

Synthesis of the Water-Soluble Ti Complex. One of the most important points of the present study was the synthesis of highly dispersed TiO_2 nanoparticles from a water-soluble Ti complex. Various water-soluble Ti complexes were synthesized using different complexing agents, as shown in Figure S1. All of the solutions of water-soluble Ti complexes were transparent and were yellow (Figure S1a–c) or orange (Figure S1d,e), depending on the complexing agent.

Hydrothermal Synthesis of TiO_2. Our aim was to synthesize highly dispersed TiO_2 nanoparticles with a particle size smaller than 25 nm for subsequent use as a raw material in the synthesis of $BaTiO_3$. The TiO_2 nanoparticles were synthesized via a hydrothermal method using water-soluble Ti complexes to achieve this purpose. Various reaction media—water, an acidic solution, and an alkaline solution—were used as the reaction media in the hydrothermal synthesis. Five different ligands were used: glycolic acid, lactic acid, citric acid, D(−)-tartaric acid, and L(+)-tartaric acid.

TiO_2 was synthesized via a hydrothermal method using water-soluble Ti complexes with glycolic acid as the ligand. X-ray diffraction (XRD) patterns and scanning electron microscopy (SEM) images for the resultant products are shown in Figure S2 and Figure 1, respectively. Rutile-type

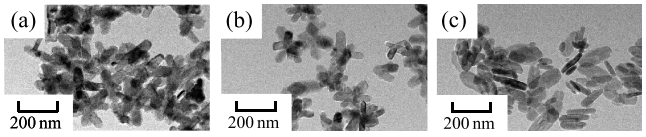

Figure 1. BF-TEM images of obtained powders via the hydrothermal method using different water-soluble complexes of Ti and glycolic acid as the ligand dissolved in a reaction medium of (a) nitric acid solution, (b) water, or (c) ammonia solution. The reaction was performed at 200 °C for 12 h.

TiO_2 was obtained when the nitric acid solution (Figure S2a) or water (Figure S2b) was used as the medium, and brookite-type TiO_2 was obtained when the ammonia solution was used (Figure S2c). The size of the rutile-type TiO_2 particles was several tens of nanometers (Figure 1a,b). The brookite-type TiO_2 particles (Figure 2a,b) were slightly larger than the rutile-type TiO_2 particles (Figure 1c).

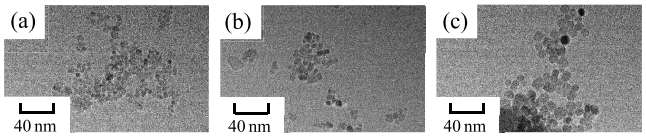

Figure 2. BF-TEM images of obtained powders via the hydrothermal method using different water-soluble complexes of Ti and lactic acid as the ligand dissolved in a reaction medium of (a) nitric acid solution, (b) water, or (c) ammonia solution. The reaction was performed at 200 °C for 12 h.

TiO_2 was next synthesized via a hydrothermal method using a water-soluble Ti complex with lactic acid as the ligand. The corresponding XRD patterns and SEM images are shown in Figure S3 and Figure 2, respectively. Anatase-type TiO_2 was obtained using the nitric acid solution (Figure S3a) or water (Figure S3b), and brookite-type TiO_2 was obtained using the ammonia solution (Figure S3c). The anatase-type TiO_2 particles were nanometer-scale fine particles (Figure 2a,b),

https://doi.org/10.1021/acsomega.1c04013
ACS Omega 2021, 6, 32517−32527

and the size of the brookite-type TiO_2 particles (Figure 2a,b) was several tens of nanometers (Figure 2c).

TiO_2 was also synthesized via a hydrothermal method using a water-soluble Ti complex with citric acid as the ligand. The corresponding XRD patterns and SEM images are shown in Figure S4 and Figure 3, respectively. All of the synthesized

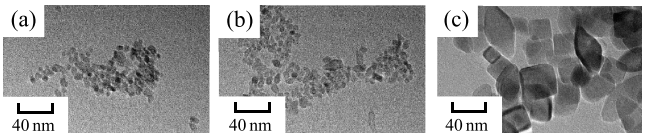

Figure 3. BF-TEM images of obtained powders via the hydrothermal method using different water-soluble complexes of Ti and citric acid as the ligand dissolved in a reaction medium of (a) nitric acid solution, (b) water, or (c) ammonia solution. The reaction was performed at 200 °C for 12 h.

powders were anatase-type TiO_2 irrespective of whether a nitric acid solution, water, or ammonia solution was used as the medium (Figure S4a−c). Fine nanosized particles were obtained when the nitric solution or water was used (Figure 3a,b). However, the particle size became large (several tens of nanometers) when ammonia solution was used (Figure 3c).

TiO_2 was then synthesized via a hydrothermal method with a water-soluble Ti complex with D(−)-tartaric acid as the ligand. The corresponding XRD patterns and SEM images are shown in Figure S5 and Figure 4, respectively. All of the

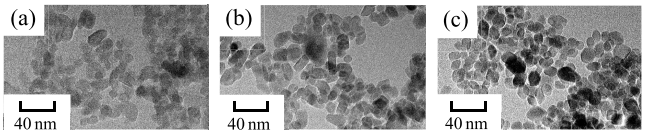

Figure 4. BF-TEM images of obtained powders via the hydrothermal method using different water-soluble complexes of Ti and D(−)-tartaric acid as the ligand dissolved in a reaction medium of (a) nitric acid solution, (b) water, or (c) ammonia solution. The reaction was performed at 200 °C for 12 h.

obtained powders were anatase-type TiO_2, irrespective of whether a nitric acid solution, water, or ammonia solution was used as the medium (Figure S5a−c). Obtained particles were fine and particles size was several tens of nanometers in all cases (Figure 4a−c).

Finally, TiO_2 was synthesized via a hydrothermal method using a water-soluble Ti complex with L(+)-tartaric acid as the ligand. The corresponding XRD patterns and SEM images are shown in Figure S6 and Figure 5, respectively. All of the obtained powders were anatase-type TiO_2, irrespective of whether a nitric acid solution, water, or ammonia solution was used as the medium (Figure S6a−c). Fine particles several tens

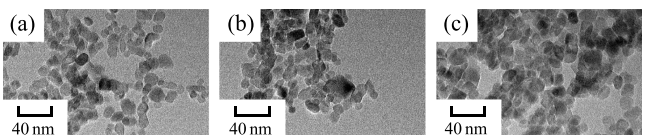

Figure 5. BF-TEM images of obtained powders via the hydrothermal method using different water-soluble complexes of Ti and L(+)-tartaric acid as the ligand dissolved in a reaction medium of (a) nitric acid solution, (b) water, or (c) ammonia solution. The reaction was performed at 200 °C for 12 h.

of nanometers in diameter were obtained in all cases (Figure 5a−c).

Figure 6 summarizes the aforementioned results. Three types of TiO_2 were obtained (anatase-TiO_2, rutile-TiO_2, and

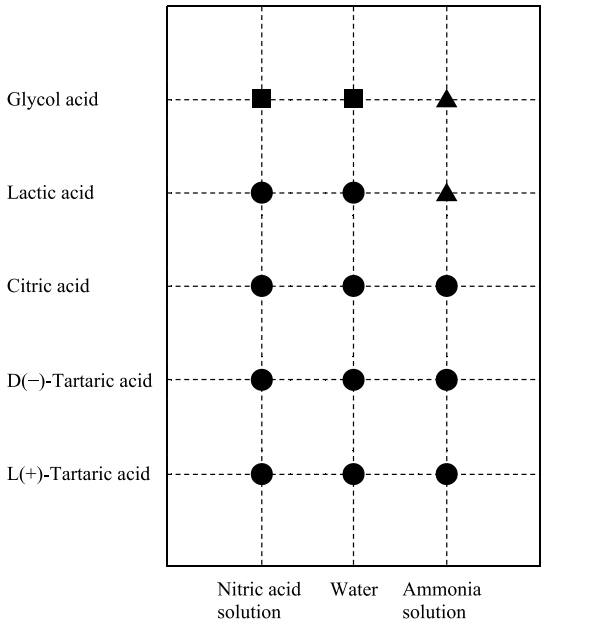

Figure 6. Formation area of TiO_2 using water-soluble Ti complexes (filled circles: anatase, filled triangles: brookite, and filled squares: rutile).

brookite-TiO_2) from a hydrothermal synthesis with water-soluble Ti complexes that contained glycolic acid, lactic acid, citric acid, D(−)-tartaric acid, or L(+)-tartaric acid as the ligand. The complexing agents differ by their carbon number. Glycolic acid has the lowest carbon number among the investigated complexing agents, whereas D(−)-tartaric acid and L(+)-tartaric acid have the largest carbon number. In addition to the complexing agent, different reaction media of a nitric acid solution, water, and an ammonia solution were investigated for the synthesis of TiO_2. The pH of the nitric acid solution was low, whereas that of the ammonia solution was high. Rutile-TiO_2 was obtained only when glycolic acid was used in the nitric acid solution or water. Brookite-TiO_2 was obtained when glycolic acid or lactic acid was used in the ammonia solution. All of the other investigated conditions resulted in anatase-TiO_2. Increasing carbon numbers in the complexing agents tended to favor the formation of anatase-TiO_2.

Hydrothermal Synthesis of $BaTiO_3$ from TiO_2. $BaTiO_3$ was synthesized via a hydrothermal method using two types of reagent TiO_2 with different particle sizes. The corresponding XRD patterns and SEM images are shown in Figure S7 and Figure 7, respectively. Figure 7a-1,b-1 shows anatase-type TiO_2 with fine (<25 nm) and large particles, respectively. When the fine TiO_2 particles were used as the raw material, the $BaTiO_3$ particles exhibited a nanocube morphology but were small (Figure 7a-2). The $BaTiO_3$ obtained using the large-particle TiO_2 as the raw material exhibited a large morphology (Figure 7b-2). These results demonstrate that the morphology of the obtained $BaTiO_3$ depended on the particle size of the TiO_2 used as the raw material.

https://doi.org/10.1021/acsomega.1c04013
ACS Omega 2021, 6, 32517−32527

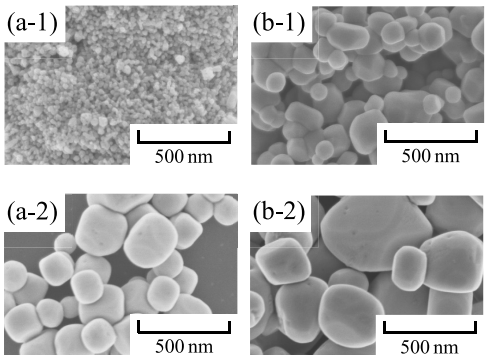

Figure 7. SEM images of obtained powders via the hydrothermal method using various commercially obtained TiO_2 particles in water. The reaction was conducted at 200 °C for 72 h, with a reaction medium of water (40 mL). Commercial TiO_2: (a-1) fine particles and (b-1) large particles. Obtained $BaTiO_3$ using commercial TiO_2: (a-2) fine particles and (b-2) large particles.

Hydrothermal Synthesis of $BaTiO_3$ Nanocubes with TiO_2 Nanoparticles Synthesized In Situ. Our objective was to synthesize highly dispersed $BaTiO_3$ nanocubes with a narrow particle size distribution. We speculated that using fine TiO_2 nanoparticles smaller than 25 nm as a raw material would lead to the formation of $BaTiO_3$ nanocubes with the desired properties. The fine TiO_2 nanoparticles were synthesized via a hydrothermal method with water-soluble Ti complexes. That is, we synthesized $BaTiO_3$ nanocubes with a narrow particle size distribution via a hydrothermal method with TiO_2 nanoparticles synthesized in situ. Five different ligands were used for the synthesis of the water-soluble Ti complexes.

First, $BaTiO_3$ was synthesized via a hydrothermal method using $Ba(OH)_2{\cdot}8H_2O$ and TiO_2 synthesized from a water-soluble Ti complex with glycolic acid as the ligand (Figure 1). The XRD patterns and SEM images for the products are shown in Figure S8 and Figure 8, respectively. All the obtained

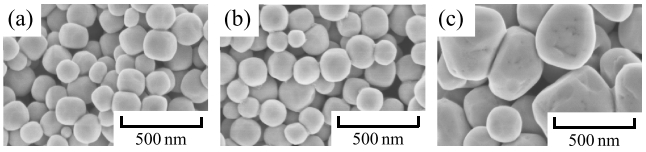

Figure 8. SEM images of obtained powders via the hydrothermal method using $Ba(OH)_2{\cdot}8H_2O$ and various TiO_2 particles synthesized as shown in Figure 1. The reaction was conducted at 200 °C for 72 h. The ligand used for the synthesis of TiO_2 was glycolic acid. Reaction medium: (a) nitric acid solution, (b) water, or (c) ammonia solution.

powders were confirmed to be $BaTiO_3$ irrespective of whether a nitric acid solution, water, or ammonia solution was used as the medium (Figure S8a–c). Cube-like $BaTiO_3$ with rounded edges were obtained when the nitric acid solution or water was used (Figure 8a,b). However, the particles became large when the ammonia solution was used as the reaction medium (Figure 8c).

Second, $BaTiO_3$ was synthesized via a hydrothermal method using $Ba(OH)_2{\cdot}8H_2O$ and TiO_2 synthesized from a water-soluble Ti complex with lactic acid as the ligand (Figure 2). The corresponding XRD patterns and SEM images are shown in Figure S9 and Figure 9, respectively. All of the obtained powders were confirmed to be $BaTiO_3$ irrespective of whether nitric acid solution, water, or ammonia solution was used as the

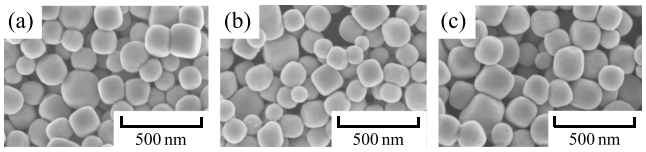

Figure 9. SEM images of obtained powders via the hydrothermal method using $Ba(OH)_2{\cdot}8H_2O$ and various TiO_2 particles synthesized as shown in Figure 2. The reaction was conducted at 200 °C for 72 h. The ligand used for the synthesis of TiO_2 was lactic acid. Reaction medium: (a) nitric acid solution, (b) water, or (c) ammonia solution.

medium (Figure S9a–c). All of the obtained powders were confirmed to be $BaTiO_3$ nanocubes (Figure 9). In the case of the $BaTiO_3$ nanocubes synthesized via a hydrothermal method using water as a reaction medium (Figure 9b), bright-field transmission electron microscopy (BF-TEM) observations (Figure S10) indicate that the average size of 200 $BaTiO_3$ nanocubes was 166 nm when measured corner to corner, corresponding to a side length of 117 nm on average. A comparison of the particle size of the $BaTiO_3$ nanocubes in Figure 7a-2 and that of the nanocubes in Figure 9b reveals that the side length of the particles of the $BaTiO_3$ nanocubes synthesized using TiO_2 synthesized in situ was smaller by 23 nm. These results provide further evidence that the TiO_2 particle size of the raw material affects the particles size of the $BaTiO_3$ nanocubes.

Third, $BaTiO_3$ was synthesized via a hydrothermal method using $Ba(OH)_2{\cdot}8H_2O$ and TiO_2 synthesized from a water-soluble Ti complex with citric acid as the ligand (Figure 3). The corresponding XRD patterns and the SEM images are shown in Figure S11 and Figure 10, respectively. All of the

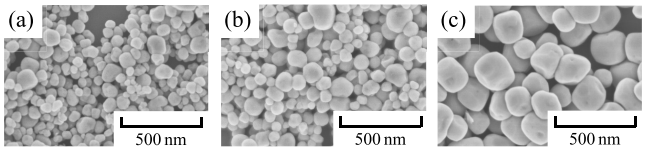

Figure 10. SEM images of obtained powders via the hydrothermal method using $Ba(OH)_2{\cdot}8H_2O$ and various TiO_2 particles synthesized as shown in Figure 3. The reaction was conducted at 200 °C or 72 h. The ligand used for the synthesis of TiO_2 was citric acid. Reaction medium: (a) nitric acid solution, (b) water, or (c) ammonia solution.

obtained powders were confirmed to be $BaTiO_3$ irrespective of whether a nitric acid solution, water, or ammonia solution was used as the medium (Figure S11a–c). Among the investigated media, the nitric acid solution was found to result in the smallest $BaTiO_3$ particles; however, the $BaTiO_3$ particles were not cubic (Figure 10a). When water was used as the reaction medium, the particles of $BaTiO_3$ were relatively small (Figure 10b), whereas the ammonia solution resulted in the growth of large particles (Figure 10c).

Fourth, $BaTiO_3$ was synthesized via a hydrothermal method using $Ba(OH)_2{\cdot}8H_2O$ and TiO_2 synthesized from a water-soluble Ti complex with D(−)-tartaric acid as the ligand (Figure 4). The corresponding XRD patterns and SEM images for the products are shown in Figure S12 and Figure 11, respectively. All of the obtained powders were confirmed to be $BaTiO_3$ irrespective of whether a nitric acid solution, water, or ammonia solution was used as the medium (Figure S12a–c). When a nitric acid solution or water was used as the reaction medium, only cube-like $BaTiO_3$ particles were obtained

https://doi.org/10.1021/acsomega.1c04013
ACS Omega 2021, 6, 32517−32527

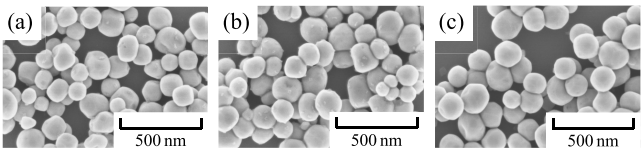

Figure 11. SEM images of obtained powders via the hydrothermal method using $Ba(OH)_2{\cdot}8H_2O$ and various TiO_2 particles synthesized as shown in Figure 4. The reaction was conducted at 200 °C for 72 h. The ligand used for the synthesis of TiO_2 was D(−)-tartaric acid. Reaction medium: (a) nitric acid solution, (b) water, or (c) ammonia solution.

(Figure 11a,b). When the ammonia solution was used as the medium, $BaTiO_3$ particles were small (Figure 11c).

Fifth and finally, $BaTiO_3$ was synthesized via a hydrothermal method using $Ba(OH)_2{\cdot}8H_2O$ and TiO_2 synthesized from a water-soluble Ti complex with L(+)-tartaric acid as the ligand (Figure 5). The corresponding XRD patterns and SEM images are shown in Figure S13 and Figure 12, respectively. The obtained $BaTiO_3$ particles were cube-like irrespective of whether the nitric acid solution, water, or the ammonia solution was used as the medium (Figure 12a−c).

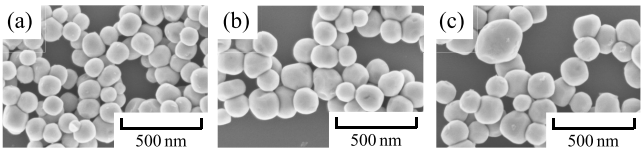

Figure 12. SEM images of obtained powders via the hydrothermal method using $Ba(OH)_2{\cdot}8H_2O$ and various TiO_2 particles synthesized as shown in Figure 5. The reaction was conducted at 200 °C for 72 h. The ligand used for the synthesis of TiO_2 was L(+)-tartaric acid. Reaction medium: (a) nitric acid solution, (b) water, or (c) ammonia solution.

We investigated the formation mechanism of $BaTiO_3$ nanocubes synthesized using TiO_2 particles with different sizes as the raw material.[22] Figure 13 shows the formation mechanism for $BaTiO_3$ nanocubes. The raw material in Figure 13a is large TiO_2 particles, and that in Figure 13b is fine TiO_2 particles. The large TiO_2 particles were not dissolved in the reaction medium before the hydrothermal synthesis was carried out (Figure 13a). During the hydrothermal synthesis, the large TiO_2 particles became small because they dissolved in the reaction medium. As the hydrothermal reaction progressed, $BaTiO_3$ nanocubes gradually nucleated, whereas the TiO_2 particles remained in the reaction medium. Therefore, the size of the $BaTiO_3$ nanocubes varied widely. As a result, $BaTiO_3$ nanocubes with a broad particle size distribution were obtained; TiO_2 did not fully dissolve in the reaction medium if the TiO_2 particles were too large.

The behavior of fine TiO_2 particles differed from that of large TiO_2 particles under the hydrothermal reaction conditions used in the synthesis of $BaTiO_3$. Fine TiO_2 was also not dissolved in the reaction medium before the hydrothermal synthesis (Figure 13b). However, during the hydrothermal synthesis, fine TiO_2 particles were completely dissolved in the reaction medium. As the hydrothermal reaction progressed, $BaTiO_3$ nanocubes nucleated. Finally, $BaTiO_3$ nanocubes were obtained with a narrow particle size distribution. The key point for the formation of $BaTiO_3$ nanocubes with a narrow particle size distribution is a large number of nuclei that form simultaneously and grow into $BaTiO_3$ nanocubes during the hydrothermal reaction.

XRD Analysis of the $BaTiO_3$ Nanocubes. In the present work, we examined five ligands for the $BaTiO_3$ synthesis. From the results in Figures 9 and 13, the best shape of the nanocube was when using lactic acid. Figure 14 shows a high-energy synchrotron XRD pattern for the $BaTiO_3$ nanocubes. The RIETAN-FP software[23] was used for a Rietveld refinement based on a *P4mm* model for $BaTiO_3$ in a tetragonal crystal system. In the present work, the wavelength of an X-ray with 0.020615 nm was used for a high-energy synchrotron XRD pattern measurement, enabling us to acquire high-resolution XRD data. The same sample that is shown in Figure 9b was used for the high-energy synchrotron XRD pattern measurement. The obtained XRD data verified a single phase of $BaTiO_3$, and the XRD results indicated that a tetragonal crystal system with a *P4mm* space group was assigned (Table 1).[24]

The pair distribution function (PDF) method was used to analyze the radial distribution from disordered materials on the basis of their powder XRD patterns and to get knowledge of the interatomic distances. A PDF analysis of the XRD pattern that was obtained using high-energy synchrotron X-rays (Figure 14) is shown in Figure 15. The results indicated Ti−O interatomic distances of 1.9 and 2.2 Å, a Ba−O interatomic distance of 2.8 Å, a Ba−Ti interatomic distance of 3.5 Å, and a Ba−Ba interatomic distance of 4.0 Å. These results suggest that there is a displacement of the Ti atom from the center of the $BaTiO_3$ unit cell, causing spontaneous polarization of the $BaTiO_3$ tetragonal crystal structure.[24]

Detailed Observation of $BaTiO_3$ Nanocubes Using electron Microscopy. $BaTiO_3$ nanocubes were observed in detail using electron microscopy. Secondary electron (SE) images, bright-field scanning transmission electron microscopy (BF-STEM) images, and high-angle annular dark-field scanning transmission electron microscopy (HAADF-STEM) images were acquired at an acceleration voltage of 200 kV (Figure 16). The $BaTiO_3$ particles were clearly confirmed to exhibit sharp-edges with corners. In addition, the $BaTiO_3$ nanocubes were highly dispersed.

Recently, the surface of perovskite structures at the atomic column level has been investigated using theoretical approaches[25−27] and electron microscopy.[28−30] Moreover, the facets of particles have also been studied.[25−30] In the present work, the surface of $BaTiO_3$ nanocubes was examined using electron microscopy. Figure 17 shows TEM results for a $BaTiO_3$ nanocube taken from the direction of [001] incidence. A single crystal of $BaTiO_3$ was identified from the TEM image (Figure 17a) and the corresponding nanobeam diffraction pattern (Figure 17b).

The atomic column of $BaTiO_3$ nanocube observed in the direction of [001] incidence is shown in Figure 18. The corresponding TEM image (Figure 17a) was used for analysis. Figure 18a-1 is a HAADF-STEM image, and Figure 18a-2 is an the annular bright-field scanning transmission electron microscopy (ABF-STEM) image. Figure 18a-1,a-2 in the middle of the array shows broad views of a $BaTiO_3$ nanocube. Figure 18b-1,b-2,d-1,d-2,f-1,f-2,h-1,h-2 shows images of the four corners of the $BaTiO_3$ nanocube. Figure 18c-1,c-2,e-1,e-2,g-1,g-2,i-1,i-2 shows images corresponding to the top, right, bottom, and left sides of the $BaTiO_3$ nanocube, respectively. The arrangement of atomic column and surface reconstruction were obtained by means of Cs-corrected HAADF-STEM and ABF-STEM images of the sides of the $BaTiO_3$ nanocube.

https://doi.org/10.1021/acsomega.1c04013
ACS Omega 2021, 6, 32517−32527

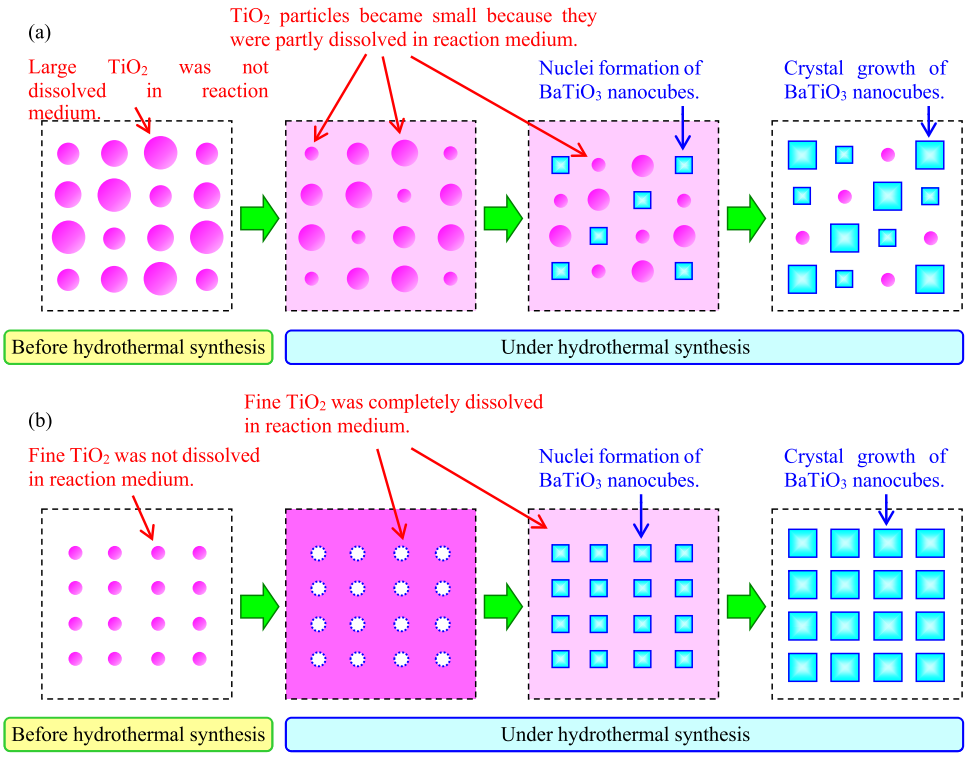

Figure 13. Formation mechanism for $BaTiO_3$ nanocubes from (a) large and (b) fine TiO_2 particles as the raw materials.

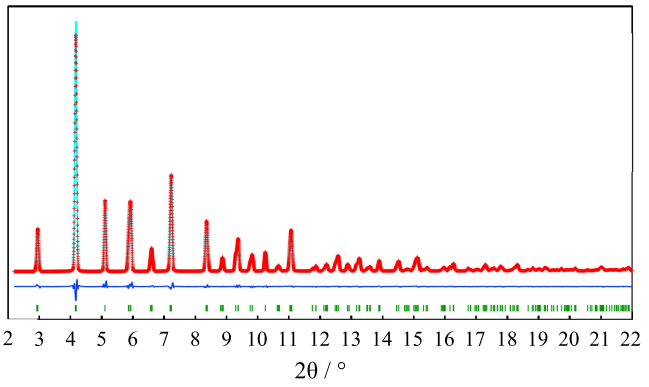

Figure 14. High-energy synchrotron XRD pattern of $BaTiO_3$ nanocubes and its Rietveld refinement. A wavelength of X-ray is 0.020615 nm. Concerning the Rietveld refinement, the recorded spectrum is shown as red cross marks and the light-blue solid line is a fit to the model for the $BaTiO_3$ phase. Red cross marks, light-blue solid lines, and blue solid lines represent observed, calculated, and differing intensities, respectively. Green ticks represent positions of the calculated Bragg reflections of the $BaTiO_3$ phase.

The contrast in HAADF-STEM images depends on the atomic number of the observed elements, where heavier elements have a higher contrast than lighter elements. This makes detecting lighter elements difficult. On the other hand, ABF-STEM allows for the detection of lighter elements such as O; accordingly, using a combination of both HAADF-STEM and ABF-STEM gives us a more complete observation that compensates for the shortcomings of both detection methods.

Figure 19 shows an observation of a $BaTiO_3$ nanocube in the direction of [110] incidence. The nanocube was confirmed to be a single crystal of $BaTiO_3$ on the basis of its TEM image (Figure 19a) and its corresponding nanobeam diffraction pattern (Figure 20b).

Table 1. Rietveld Refinement of the Structural Parameters of the High-Energy Synchrotron XRD Pattern

$BaTiO_3$, *P4mm* model						
		powder XRD				
atom	site	*x*	*y*	*z*	occupancy	B_{iso}
Ba	1*a*	0	0	0	1	0.331 (4)
Ti	1*b*	1/2	1/2	0.4699	1	0.056 (7)
O1	1*b*	1/2	1/2	0.9890	1	0.212 (54)
O2	2*c*	1/2	0	0.4654	2	0.088 (33)
a/Å		3.98592 (7)				
c/Å		4.02376 (8)				
R_{wp}/%		5.876				
R_p/%		4.112				

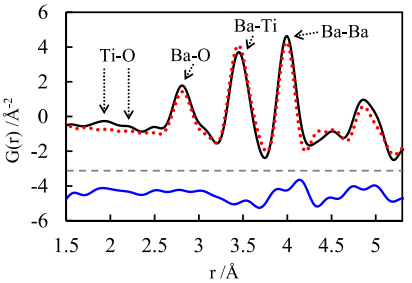

Figure 15. PDF analysis of the XRD pattern obtained by means of high-energy synchrotron X-rays as shown in Figure 14. Concerning the PDF analysis, the recorded spectrum is shown as a black solid line and red circles are the fit to recorded spectrum. The black solid line, red circle marks, and blue solid lines represent observed, calculated, and differing intensities, respectively.

Figure 20 shows HAADF-STEM (Figure 20a-1) and ABF-STEM (Figure 20a-2) observations of a $BaTiO_3$ nanocube in the direction of [110] incidence. Figure 20a-1,a-2 in the

https://doi.org/10.1021/acsomega.1c04013
ACS Omega 2021, 6, 32517−32527

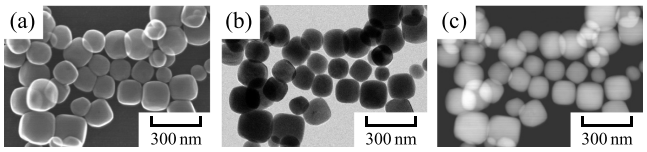

Figure 16. (a) SE, (b) BF-STEM, and (c) HAADF-STEM images of obtained powders via the hydrothermal method using various TiO_2 particles synthesized as shown in Figure 9b.

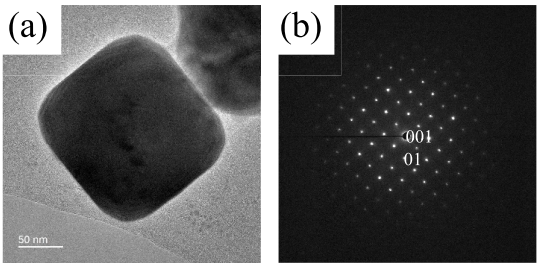

Figure 17. Observations of a $BaTiO_3$ nanocube from the [001] direction of incidence. The TEM image and the corresponding nanobeam electron diffraction pattern were acquired at an accelerating voltage of 200 kV by means of an instrument equipped with a Cs corrector. (a) TEM image and (b) nanobeam diffraction.

middle of the array shows broad views of the $BaTiO_3$ nanocube. The direction of [110] incidence shows a contrast on the nanocube that indicates that this incidence is taken through a corner. The brighter section indicates more atoms, and the darker sections indicate less atoms. On the other hand, an image that has little contrast indicates a face on incidence, for example, Figure 18. Figure 20b-1,b-2,d-1,d-2,g-1,g-2 shows images of the corners of the $BaTiO_3$ nanocube. Figure 20c-1,c-2,e-1,e-2,f-1,f-2 shows images of the top, right, and bottom sides of the $BaTiO_3$ nanocube, respectively. A Cs-corrected HAADF-STEM image and ABF-STEM image of the atomic column arrangement and surface reconstruction were used to observe the sides of the $BaTiO_3$ nanocube. Notably, one of the

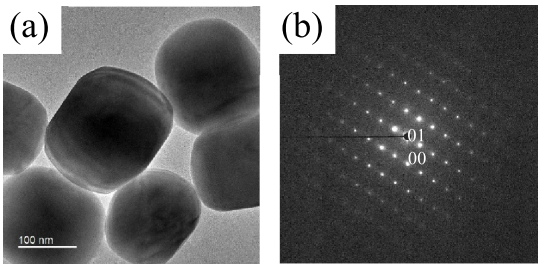

Figure 19. $BaTiO_3$ nanocubes observation from the [110] direction of incidence. The (a) TEM image and (b) corresponding nanobeam electron diffraction pattern were acquired at an accelerating voltage of 200 kV by means of an instrument equipped with a Cs corrector.

atomic positions of O is overlapped with the atomic position of Ti in the direction of [001] incidence (Figure 18). On the other hand, a different O atom position is overlapped with the atomic position of Ba in the direction of [110] incidence (Figure 20). Therefore, all the atomic positions of the O atoms are clearly observed using the images in both the directions of [001] and [110].

We tried to examine the surface of $BaTiO_3$ nanocube; however, the electron beam could not transmit through the $BaTiO_3$ nanocube well, so the surface reconstruction of cube-like $BaTiO_3$ nanoparticles with facets was examined through elemental analysis. Figure S14 shows observations of cube-like $BaTiO_3$ in the direction of [001] incidence. From the TEM results, a single crystal of $BaTiO_3$ nanocube was clarified (Figure S14a), with the corresponding nanobeam diffraction pattern (Figure S14b). Figure S15 shows HAADF-STEM observations and EELS analysis of a cube-like $BaTiO_3$ in the direction of [001] incidence, as is visible in the corresponding same sample in Figure S14. Here, the constituent element of $BaTiO_3$ is three (Ba, Ti, and O), and analysis of Ba and O can be performed using energy dispersive X-ray spectroscopy, although analysis of Ti is more difficult due to the Lα lines of Ba overlapping the Kα lines of Ti. On the other hand, electron energy-loss spectroscopy (EELS) allows for the elemental

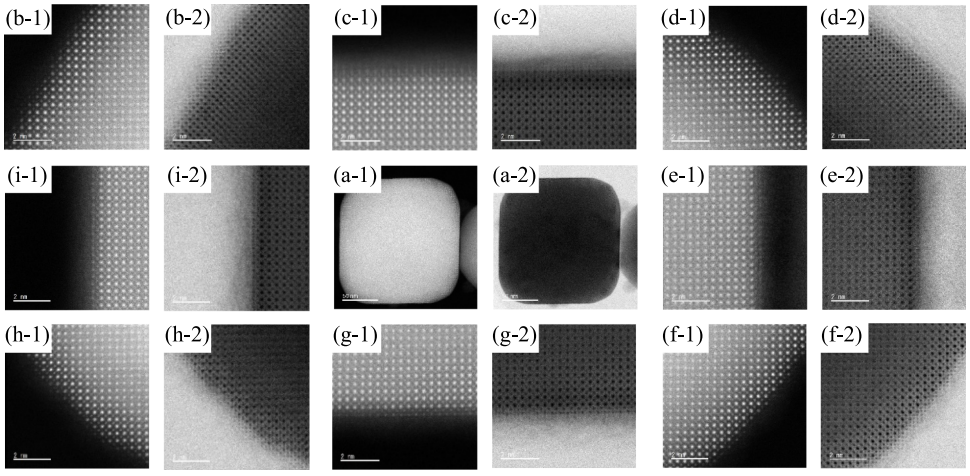

Figure 18. Observations of atomic columns in $BaTiO_3$ nanocubes in the [001] direction of incidence. STEM images were acquired at an accelerating voltage of 200 kV using an instrument equipped with a Cs corrector. HAADF-STEM images: (a-1) whole particle, (b-1) top-left corner of the particle, (c-1) top of the particle, (d-1) top-right corner of the particle, (e-1) right-hand side of the particle, (f-1) bottom-right corner of the particle, (g-1) bottom of the particle, (h-1) bottom-left corner of the particle, and (i-1) left-hand side of the particle. ABF-STEM images: (a-2) whole particle, (b-2) top-left corner of the particle, (c-2) top of the particle, (d-2) top-right corner of the particle, (e-2) right-hand side of the particle, (f-2) bottom-right corner of the particle, (g-2) bottom of the particle, (h-2) bottom-left corner of the particle, and (i-2) left-hand side of the particle.

https://doi.org/10.1021/acsomega.1c04013
ACS Omega 2021, 6, 32517−32527

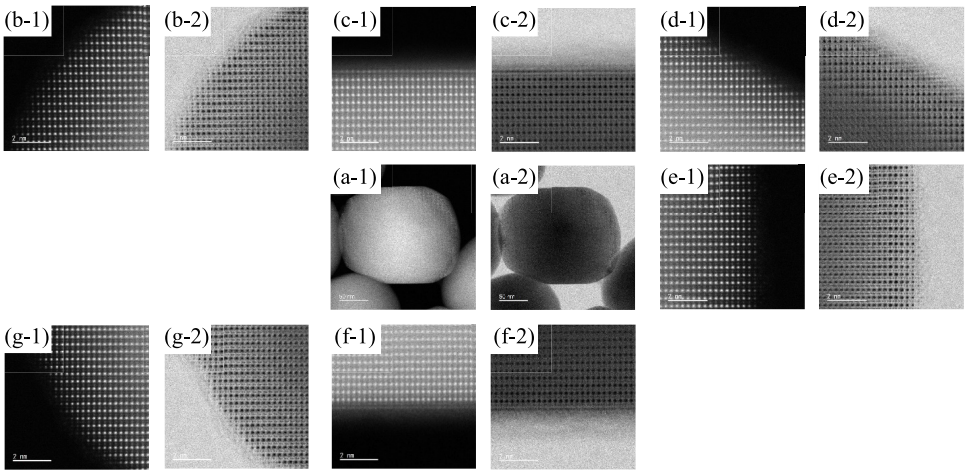

Figure 20. Observations of atomic columns in a $BaTiO_3$ nanocube in the [110] direction of incidence. STEM images were acquired at an accelerating voltage of 200 kV on an instrument equipped with a Cs corrector. HAADF-STEM images: (a-1) whole particle, (b-1) top-left corner of the particle, (c-1) top of the particle, (d-1) top-right corner of the particle, (e-1) right-hand side of the particle, (f-1) bottom of the particle, and (g-1) bottom-left corner of the particle. ABF-STEM images: (a-2) whole particle, (b-2) top-left corner of the particle, (c-2) top of the particle, (d-2) top-right corner of the particle, (e-2) right-hand side of the particle, (f-2) bottom of the particle, and (g-2) bottom-left corner of the particle.

analysis of Ti because Ti peaks do not overlap Ba peaks in EELS spectra. Accordingly, elemental analysis of a $BaTiO_3$ nanocube surface was performed using EELS. Ba and Ti are indicated by green and red, respectively. Elemental analyses of Ba and Ti were carried out on the basis of the EELS peaks for Ti and Ba. Observation of the atomic column of HAADF-STEM and their EELS analyses were conducted on the top and left side of the cube-like $BaTiO_3$ nanoparticle. A regular arrangement of Ba and Ti columns was clearly observed inside the cube-like $BaTiO_3$ nanoparticle, as well as with surface reconstruction made up of Ti columns with no Ba columns at the outermost surface on every side of the cube-like $BaTiO_3$ nanoparticles. As a result, the surface reconstruction of the cube-like $BaTiO_3$ nanoparticles was confirmed from Figure S14.

A three-dimensional (3D) moving image (Supporting Information 3D-1), which is constructed from HAADF-STEM images of Figure S16, shows electron tomography results for the $BaTiO_3$ nanocubes, as constructed by acquiring HAADF-STEM images at various angles and subsequently rendering the volume and isosurface, which can provide information about the interior and surface of substances, respectively (Figure 21).[31] Clearly, the $BaTiO_3$ nanocubes exhibit a 3D cubic morphology with defined edges and facets clearly exposed. In addition, the interior of the $BaTiO_3$ nanocubes was observed from a slice image along the intersection of the *x*, *y*, and *z* axes. Using electron tomography, we confirmed that $BaTiO_3$ nanocubes were obtained without voids. In addition, 3D analysis of other $BaTiO_3$ nanocubes is shown in Figure S17. Supporting Information 3D-2 shows a 3D moving image of the $BaTiO_3$ nanocubes as constructed from HAADF-STEM images of Figure S18. The voidless $BaTiO_3$ nanocubes were indicated from Figures S17 and S18.

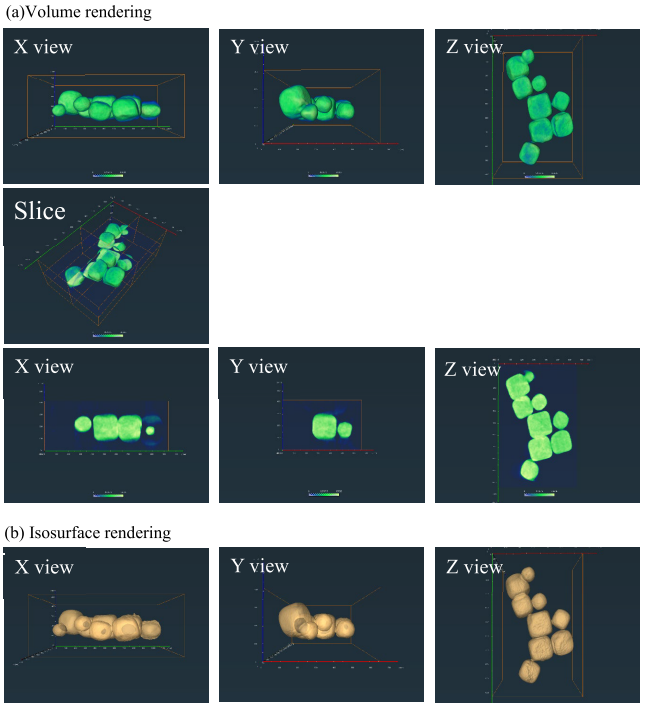

Figure 21. Electron tomography observations were performed using a scanning transmission electron microscope equipped with a Cs corrector as shown in Figure S16. $BaTiO_3$ nanocubes were imaged at an accelerating voltage of 200 kV. Regarding the 3D tomography of $BaTiO_3$ nanocubes, the tilt series consisted of 51 projections with a tilt range of ±75°; the interval of the projection was 3°. (a) Volume rendering and (b) isosurface rendering.

CONCLUSIONS

We synthesized $BaTiO_3$ with an average particle size of less than 25 nm using a hydrothermal method using water as a reaction medium with fine TiO_2 particles as a raw material. A key point for the morphology control of $BaTiO_3$ is the particle size and particle size distribution of the TiO_2. Highly dispersed TiO_2 nanoparticles with a particle size less than 25 nm are difficult to obtain from commercial sources. We therefore synthesized highly dispersed TiO_2 below 25 nm using a hydrothermal method. In addition, we controlled the structure of the TiO_2 as anatase, rutile, or brookite depending on the water-soluble Ti complex and the hydrothermal conditions used for the in situ synthesis of TiO_2.

https://doi.org/10.1021/acsomega.1c04013
ACS Omega 2021, 6, 32517−32527

We subsequently hydrothermally synthesized highly dispersed $BaTiO_3$ nanocubes with a narrow size distribution using the previously synthesized TiO_2 as the raw material. The particle size of the $BaTiO_3$ was confirmed to be 117 nm on the basis of measurements of its particle size distribution. The size of the $BaTiO_3$ crystallites was consistent with its average particle size. The key to synthesizing highly dispersed $BaTiO_3$ nanocubes with a narrow size distribution is the size of the TiO_2 particles, not their structure. In addition, surface reconstruction of the obtained $BaTiO_3$ nanocube was confirmed via electron microscopy observations, which identified the outermost surface as being composed of a Ti layer.

Given the aforementioned results, the present study clarified that the particle size of $BaTiO_3$ nanocubes depends on the particle size of TiO_2 used as the raw material and that $BaTiO_3$ particles with a narrow size distribution are obtained when TiO_2 raw-material particles have a narrow size distribution.

EXPERIMENTAL SECTION

Raw Materials. The following raw materials were used for the synthesis of $BaTiO_3$: titanium (Ti; 99.9% purity; Kojundo Chemical Laboratory Co., Ltd., Saitama, Japan); nitric acid (HNO_3; 60.0−61.0% purity; Kanto Chemical Co., Inc., Tokyo, Japan); ammonia solution (NH_3; 28.0−30.0% purity; Kanto Chemical Co., Inc., Tokyo, Japan); hydrogen peroxide (H_2O_2; 30.0−35.5% purity; Kanto Chemical Co., Inc., Tokyo, Japan); lactic acid [$CH_3CH(OH)COOH$; 85.0−92.0% purity; Kanto Chemical Co., Inc., Tokyo, Japan]; glycolic acid ($HOCH_2COOH$; >98.0% purity; Kanto Chemical Co., Inc., Tokyo, Japan); citric acid [$HOOCCH_2C(OH)(COOH)$-CH_2COOH; >99.0% purity; Kanto Chemical Co., Inc., Tokyo, Japan]; D(−)-tartaric acid [$HOOC(CHOH)_2COOH$; >99.0% purity; Kanto Chemical Co., Inc., Tokyo, Japan]; L(+)-tartaric acid [$HOOC(CHOH)_2COOH$; >99.5% purity; Kanto Chemical Co., Inc., Tokyo, Japan]; anatase-type TiO_2 (particle size: <25 nm; 99.7% purity; Sigma-Aldrich, St. Louis, MO, U.S.A.); anatase-type TiO_2 (99.8% purity; Sigma-Aldrich, St. Louis, MO, U.S.A.); barium hydroxide octahydrate [$Ba(OH)_2 \cdot 8H_2O$; 99% purity; Kojundo Chemical Laboratory Co., Ltd., Saitama, Japan]; acetic acid (CH_3COOH; 99.7% purity; Kanto Chemical Co., Inc., Tokyo, Japan); and ethanol (C_2H_5OH; 99.5% purity; Kanto Chemical Co., Inc., Tokyo, Japan).

Synthesis of Water-Soluble Ti Complexes. Figure S19a shows the flowchart of the synthesis of the water-soluble Ti complex. Ti metal powder (10 mmol) was placed in a beaker followed by the sequential addition of 40 mL of H_2O_2 solution and 10 mL of ammonia solution to the beaker. The beaker was stored in an ice bath, and the Ti metal was dissolved in the mixture solution of H_2O_2 and ammonia. After the Ti metal was dissolved, a yellow transparent solution containing the Ti-peroxo complex was obtained. Thereafter, a complexing agent [lactic acid, glycolic acid, citric acid, D(−)-tartaric acid, or L(+)-tartaric acid] was added to the solution. The amount of ligand was 30 mmol lactic acid, 27 mmol glycolic acid, 10 mmol citric acid, 10 mmol D(−)-tartaric acid, or 10 mmol L(+)-tartaric acid, respectively. To remove excess H_2O_2 and NH_3, the solution was left at room temperature overnight and then heated to 80 °C until a gel-like solid substance had formed. The gel-like solid substance was dissolved in water, and an aqueous solution of the Ti complex was obtained.

Hydrothermal Synthesis of TiO_2 Nanoparticles. Figure S19b shows the flowchart of hydrothermal synthesis of TiO_2 nanoparticles. The TiO_2 nanoparticles were synthesized via a hydrothermal method. A water-soluble Ti-complex aqueous solution (40 mL) was added to a Teflon reactor that was subsequently put into a stainless-steel autoclave that had 100 mL of internal volume. Then, the hydrothermal reaction was carried out at 200 °C for 12 h. Thereafter, we cooled the autoclave to room temperature. We collected the resultant powder by centrifugation at 10,000 rpm and rinsed it with water for three cycles and ethanol for two cycles. Finally, the resultant powder was dried at 80 °C in a drying oven.

Hydrothermal Synthesis of $BaTiO_3$ Nanocubes. Figure S19c shows the flowchart of the hydrothermal synthesis of $BaTiO_3$ nanocubes. $BaTiO_3$ nanocubes were synthesized using a hydrothermal method.[1] TiO_2; $Ba(OH)_2 \cdot 8H_2O$; and a reaction medium of water, nitric acid solution, or ammonia water were added to a Teflon reactor. The raw materials and reaction media were stirred at 350 rpm for 5 min; the resultant mixture was placed into a stainless-steel autoclave that had 100 mL of internal volume. The hydrothermal reaction was then carried out at 200 °C for 72 h. Thereafter, the autoclave was cooled to room temperature. We collected the resultant powder by centrifugation at 10,000 rpm, rinsed it with water for three cycles and ethanol for two cycles, and then dried it at 80 °C in a drying oven.

Acetic Acid Treatment. To remove the barium carbonate ($BaCO_3$) byproduct, an acetic acid treatment was performed. First, the concentration of the acetic acid aqueous solution was adjusted to 0.69 mol·dm^{-3}; then 50 mL of this solution was combined with 2 g of the product, and the resultant mixture was stirred at 350 rpm for 5 min. The product was collected by means of a centrifugal separator at 10,000 rpm, rinsed with water for three cycles and ethanol for two cycles, and then dried overnight at 80 °C in a drying oven.

Characterization of the Obtained Powders. XRD measurements were conducted by means of an Ultima IV diffractometer (Rigaku Co., Tokyo, Japan) equipped with a Cu Kα radiation source (wavelength: 0.15418 nm) operating at 40 kV and 30 mA. Samples were scanned at room temperature over the 2θ range from 10 to 80°. The products of anatase-type TiO_2, rutile-type TiO_2, and brookite-type TiO_2 were then assigned using JCPDS cards 21-1272, 1-1292, and 29-1360, respectively. High-energy synchrotron XRD measurements were performed at SPring-8 (Hyogo, Japan). The data were obtained in transmission mode at the SPring-8 BL22XU beamline by means of high-energy X-rays with a wavelength of 0.020615 nm. Short- and long-range structural parameters were refined by means of the Rietveld technique and the RIETAN-FP program.[23] SE images of the powders were acquired with SEM using an instrument (SU-4800; Hitachi High-Tech Corporation, Tokyo, Japan) operating at an accelerating voltage of 3 kV. STEM was performed with SE, bright-field (BF), and HAADF detectors by means of an instrument (HD-2700; Hitachi High-Tech Corporation, Tokyo, Japan) operating at a 200 kV acceleration voltage. In addition, TEM observations and its nanobeam diffraction patterns as well as HAADF-STEM and ABF-STEM observations were conducted by means of a JEM-ARM200CF (JEOL Ltd., Tokyo, Japan) operating at an accelerating voltage of 200 kV and equipped with a cold field emission gun and a Cs corrector to view the atomic columns of $BaTiO_3$. Elemental analysis was performed using a JEOL JEM-ARM200CF equipped with an EELS. In regard to the accelerating voltage, 200 kV has high resolution for the observation of the atomic

https://doi.org/10.1021/acsomega.1c04013
ACS Omega 2021, 6, 32517−32527

columns in contrast with 80 kV, whereas 80 kV is suitable for EELS elemental mapping as it can be conducted over a long duration of time. A long duration observation can damage the $BaTiO_3$ nanoparticle if seen at an accelerating voltage of 200 kV. Accordingly, in the STEM observations including the EELS elemental mapping, 80 kV was used with an accelerating voltage due to the lower risk of damage to the $BaTiO_3$ nanoparticle.

■ ASSOCIATED CONTENT

Supporting Information

The Supporting Information is available free of charge at https://pubs.acs.org/doi/10.1021/acsomega.1c04013.

XRD patterns, STEM images, and EELS analyses of $BaTiO_3$ (PDF)

3D moving image constructed from HAADF-STEM images of Figure S16 (MP4)

3D moving image constructed from HAADF-STEM images of Figure S18 (MP4)

■ AUTHOR INFORMATION

Corresponding Author

Kouichi Nakashima − *Department of Materials Science and Engineering, Graduate School of Science and Engineering, Ibaraki University, Hitachi, Ibaraki 316-8511, Japan;* orcid.org/0000-0001-5588-2168; Email: kouichi.nakashima.pilot@vc.ibaraki.ac.jp

Authors

Kouta Hironaka − *Department of Materials Science and Engineering, Graduate School of Science and Engineering, Ibaraki University, Hitachi, Ibaraki 316-8511, Japan*

Kazuma Oouchi − *Department of Materials Science and Engineering, Graduate School of Science and Engineering, Ibaraki University, Hitachi, Ibaraki 316-8511, Japan*

Mao Ajioka − *Department of Biomolecular Functional Engineering, College of Engineering, Ibaraki University, Hitachi, Ibaraki 316-8511, Japan*

Yoshio Kobayashi − *Department of Materials Science and Engineering, Graduate School of Science and Engineering, Ibaraki University, Hitachi, Ibaraki 316-8511, Japan*

Yasuhiro Yoneda − *Reaction Dynamics Research Division, Japan Atomic Energy Agency, Sayo-cho, Hyogo 679-5148, Japan*

Shu Yin − *Institute of Multidisciplinary Research for Advanced Materials, Tohoku University, Sendai 980-8577, Japan;* orcid.org/0000-0002-5449-4937

Masato Kakihana − *SANKEN (The Institute of Scientific and Industrial Research), Osaka University, Ibaraki, Osaka 567-0047, Japan*

Tohru Sekino − *SANKEN (The Institute of Scientific and Industrial Research), Osaka University, Ibaraki, Osaka 567-0047, Japan;* orcid.org/0000-0002-6605-9166

Complete contact information is available at: https://pubs.acs.org/10.1021/acsomega.1c04013

Author Contributions

Kouichi Nakashima conceived and designed the overall project. Samples were synthesized and characterized by Kouta Hironaka, Kazuma Oouchi, and Mao Ajioka. Synchrotron XRD pattern was measured and Rietveld refinement was carried out by Yasuhiro Yoneda. Yoshio Kobayashi, Shu Yin, Masato Kakihana, and Tohru Sekino contributed to discussions and developed the concept of the present research.

Funding

This work was supported by JSPS KAKENHI Grant JP19K05644 and by the Asahi Glass Foundation.

Notes

The authors declare no competing financial interest.

■ ACKNOWLEDGMENTS

This work was performed under the Research Program of the "Dynamic Alliance for Open Innovation Bridging Human, Environment and Materials" in the "Network Joint Research Center for Materials and Devices", Grant 20214038, and was supported by "The JAEA and QST Advanced Characterization Nanotechnology Platforms" of the Ministry of Education, Culture, Sports, Science and Technology (MEXT), Japan, Grant JPMXP09A19AE0006. This work was also supported by the Advanced Characterization Platform of the Nanotechnology Platform Japan sponsored by the MEXT, Japan, Grants JPMXP09A20KU0341 and JPMXP09A21NM0005. We are grateful to Mr. Takaaki Toriyama of Kyushu University for helpful support in the STEM analysis and Ms. Noriko Isaka of the National Institute for Materials Science for helpful support in the 3D visualization using the electron tomography method. We are also grateful to Mr. Shunsuke Kayamori for his helpful support with SE, BF-STEM, and HAADF-STEM observations at Tohoku University.

■ REFERENCES

(1) Nakashima, K.; Onagi, K.; Kobayashi, K.; Ishigaki, T.; Ishikawa, Y.; Yoneda, Y.; Yin, S.; Kakihana, M.; Sekino, T. Stabilization of Size-controlled $BaTiO_3$ Nanocubes via Precise Solvothermal Crystal Growth and Their Anomalous Surface Compositional Reconstruction. *ACS Omega* **2021**, *6*, 9410−9425.

(2) Adireddy, S.; Lin, C.; Cao, B.; Zhou, W.; Caruntu, G. Solution-Based Growth of Monodisperse Cube-like $BaTiO_3$ Colloidal Nanocrystals. *Chem. Mater.* **2010**, *22*, 1946−1948.

(3) Mimura, K.-I. Processing of Dielectric Nanocube 3D-assemblies and Their High Electrical Properties for Next-generation Devices. *J. Ceram. Soc. Jpn.* **2016**, *124*, 848−854.

(4) Costanzo, T.; McCracken, J.; Rotaru, A.; Caruntu, G. Quasi-Monodisperse Transition-Metal=Doped $BaTiO_3$ (M = Cr, Mn, Fe, Co) Colloidal Nanocrystals with Multiferroic Properties. *ACS Appl. Nano Mater.* **2018**, *1*, 4863−4874.

(5) Ding, L.; Yang, S.; Liang, Z.; Qian, X.; Chen, X.; Cui, H.; Tian, J. TiO_2 nanobetls with anatase/rutile heterophase junctions for highly efficient photocatalytic overall water splitting. *J. Colloid Interface Sci.* **2020**, *567*, 181−189.

(6) Qin, Y.; Guo, Y.; Liang, Z.; Xue, Y.; Zhang, X.; Yang, L.; Tian, J. Au nanorods decorated TiO_2 nanobelts with enhanced full solar spectrum photocatalytic antibacterial activity and the sterilization file cabinet application. *Chin. Chem. Lett.* **2021**, *32*, 1523−1526.

(7) Liang, Z.; Bai, X.; Hao, P.; Guo, Y.; Xue, Y.; Tian, J.; Cui, H. Full solar spectrum photocatalytic oxygen evolution by carbon-coated TiO_2 hierarchical nanotubes. *Appl. Catal., B* **2019**, *243*, 711−720.

(8) Li, X.; Ma, X.; Lang, X. Blue light-powered hydroxynaphthoic acid-titanium dioxide photocatalysis for the selective aerobic oxidation of amines. *J. Colloid Interface Sci.* **2021**, *602*, 534−543.

(9) Li, X.; Xu, H.; Shi, J.-L.; Hao, H.; Yuan, H.; Lang, X. Salicylic acid complexed with TiO2 for visible light-driven selective oxidation of amines into imines with air. *Appl. Catal., B* **2019**, *244*, 758−766.

(10) Hao, H.; Shi, J.-L.; Xu, H.; Li, X.; Lang, X. *N*-hydroxyphthalimide-TiO_2 complex visible light photocatalysis. *Appl. Catal., B* **2019**, *246*, 149−155.

(11) Kakihana, M.; Tada, M.; Shiro, M.; Petrykin, V.; Osada, M.; Nakamura, Y. Structure and Stability of Water Soluble $(NH_4)_8[Ti_4(C_6H_4O_7)_4(O_2)_4]\cdot 8H_2O$. *Inorg. Chem.* **2001**, *40*, 891−894.
(12) Kakihana, M.; Tomita, K.; Petrykin, V.; Tada, M.; Sasaki, S.; Nakamura, Y. Chelating of Titanium by Lactic Acid in the Water-Soluble Diammonium Tris(2-hydroxypropionato)titanate(IV). *Inorg. Chem.* **2004**, *43*, 4546−4548.
(13) Tomita, K.; Petrykin, V.; Kobayashi, M.; Shiro, M.; Yoshimura, M.; Kakihana, M. A Water-Soluble Titanium Complex for the Selective Synthesis of Nanocrystalline Brookite, Rutile, and Anatase by a Hydrotherma Method. *Angew. Chem., Int. Ed.* **2006**, *45*, 2378−2381.
(14) Kobayashi, M.; Petrykin, V. V.; Kakihana, M.; Tomita, K.; Yoshimura, M. One-Step Synthesis of TiO_2(B) Nanoparticles from a Water-Soluble Titanium Complex. *Chem. Mater.* **2007**, *19*, 5373−5376.
(15) Kobayashi, M.; Petrykin, V.; Kakihana, M.; Tomita, K. Hydrothermal Control of Rutile Nanoparticles in a Hydrothermal Synthesis from Water-Soluble Titanium Complex Aqueous Solution. *J. Ceram. Soc. Jpn.* **2007**, *115*, 835−839.
(16) Kobayashi, M.; Petrykin, V.; Kakihana, M.; Tomita, K. Hydrothermal Synthesis and Photocatalytic Actively of Whisker-Like Rutile-Type Titanium Dioxide. *J. Am. Ceram. Soc.* **2009**, *92*, S21−S26.
(17) Yamamoto, K.; Tomita, K.; Fujita, K.; Kobayashi, M.; Petrykin, V.; Kakihana, M. Synthesis of TiO_2(B) Using Glycolato Titanium Complex and Post-synthetic Hydrothermal Crystal Growth of TiO_2(B). *J. Cryst. Growth* **2009**, *311*, 619−622.
(18) Kakihana, M.; Kobayashi, M.; Tomita, K.; Petrykin, V. Application of Water-Soluble Titanium Complexes as Precursors for Synthesis of Titanium-Containing Oxides via Aqueous Solution Processes. *Bull. Chem. Soc. Jpn.* **2010**, *83*, 1285−1308.
(19) Kobayashi, M.; Petrykin, V.; Tomita, K.; Kakihana, M. Hydrothermal Synthesis of Brookite-type Titanium Dioxide with Snowflake-like Nanostructures Using a Water-Soluble Citratoperoxotitanate Complex. *J. Cryst. Growth* **2011**, *337*, 30−37.
(20) Kobayashi, M.; Kato, H.; Kakihana, M. Synthesis of Spindle and Square Bipyramid-shaped Anatase-type Titanium Dioxide Crystals by a Solvothermal Method using Ethylendiamine. *J. Ceram. Soc. Jpn.* **2012**, *120*, 494−499.
(21) Kobayashi, M.; Kato, H.; Kakihana, M. Synthesis of Titanium Dioxide Nanocrystals with Controlled Crystal- and Micro-Structures from Titanium Complexes. *Nanomater. Nanotechnol.* **2013**, *3*, 1−10.
(22) Zhan, H.; Yang, X.; Wang, C.; Chen, J.; Wen, Y.; Liang, C.; Greer, H. F.; Wu, M.; Zhou, W. Multiple Nucleation and Crystal Growth of Barium Titanate. *Cryst. Growth Des.* **2012**, *12*, 1247−1253.
(23) Izumi, F.; Momma, K. Three-Dimensional Visualization in Powder Diffraction. *Solid State Phenom.* **2007**, *130*, 15−20.
(24) Smith, M. B.; Page, K.; Siegrist, T.; Redmond, P. L.; Walter, E. C.; Seshadri, R.; Brus, L. E.; Steigerwald, M. L. Crystal Structure and the Paraelectric-to-Ferroelectric Phase Transition of Nanoscale $BaTiO_3$. *J. Am. Chem. Soc.* **2008**, *130*, 6955−6963.
(25) Koocher, N. Z.; Martirez, J. M. P.; Rappe, A. M. Theoretical Model of Oxidative Adsorption of Water on a Highly Reduced Reconstructed Oxide Surface. *J. Phys. Chem. Lett.* **2014**, *5*, 3408−3414.
(26) Rivera Rocabado, D. S.; Ishimoto, T.; Koyama, M. Theoretical Approach to the Sulfidation of the $BaTiO_3$(001) Surfaces and Its Effect on the H_2 Oxidation Reaction and CH_4 Sequential Dissociation. *J. Phys. Chem. C* **2018**, *122*, 1437−1446.
(27) Erdman, N.; Warschkow, O.; Asta, M.; Poeppelmeier, K. R.; Ellis, D. E.; Marks, L. D. Surface Structure of $SrTiO_3$ (001): A TiO_2-rich Reconstruction with a c(4×2) Unit Cell. *J. Am. Chem. Soc.* **2003**, *125*, 10050−10056.
(28) Shetty, S.; Sinha, S. K.; Ahmad, R.; Singh, A. K.; van Tendeloo, G.; Ravishankar, N. Existence of Ti^{2+} States on the Surface of Heavily Reduced $SrTiO_3$ Nanocubes. *Chem. Mater.* **2017**, *29*, 9887−9891.
(29) Du, H.; Jia, C.-L.; Mayer, J. Surface Atomic Structure and Growth Mechanism of Monodisperse {1 0 0}-Faceted Strontium Titanate Zirconate Nanocubes. *Chem. Mater.* **2016**, *28*, 650−656.
(30) Matsukawa, M.; Ishikawa, R.; Hisatomi, T.; Moriya, Y.; Shibata, N.; Kubota, J.; Ikuhara, Y.; Domen, K. Enhancing Photocatalytic Activity of $LaTiO_2N$ by Removal of Surface Reconstruction Layer. *Nano Lett.* **2014**, *14*, 1038−1041.
(31) Scott, M. C.; Chen, C.-C.; Mecklenburg, M.; Zhu, C.; Xu, R.; Ercius, P.; Dahmen, U.; Regan, B. C.; Miao, J. Electron tomography at 2.4-ångström resolution. *Nature* **2012**, *483*, 444−447.

https://doi.org/10.1021/acsomega.1c04013
ACS Omega 2021, 6, 32517−32527